

Image reconstruction algorithms for electrical capacitance tomography based on ROF model using new numerical techniques

This content has been downloaded from IOPscience. Please scroll down to see the full text.

2017 Meas. Sci. Technol. 28 035404

(<http://iopscience.iop.org/0957-0233/28/3/035404>)

View [the table of contents for this issue](#), or go to the [journal homepage](#) for more

Download details:

IP Address: 58.60.1.3

This content was downloaded on 19/08/2017 at 14:18

Please note that [terms and conditions apply](#).

You may also be interested in:

[A sparsity reconstruction algorithm for electrical capacitance tomography based on modified Landweber iteration](#)

Jiamin Ye, Haigang Wang and Wuqiang Yang

[Characterization of a multi-plane electrical capacitance tomography sensor with different numbers of electrodes](#)

Jiamin Ye, Haigang Wang and Wuqiang Yang

[Fast and robust 3D electrical capacitance tomography](#)

Y Li and D J Holland

[Image reconstruction inelectrical capacitance tomography](#)

H Yan, L J Liu, H Xu et al.

[An Imaging Method for Electrical Capacitance Tomography Based on Projections Multiplication](#)

A Martínez Olmos, E Castillo, F Martínez-Martí et al.

[Evaluation of electrical capacitance tomography sensor based on the coupling of fluid field and electrostatic field](#)

Jiamin Ye, Haigang Wang and Wuqiang Yang

[Image reconstruction by nonlinear Landweber iteration for complicated distributions](#)

Yi Li and Wuqiang Yang

[An image reconstruction algorithm based on new objective functional for ECT](#)

Jing Lei, Shi Liu, Zhihong Li et al.

Image reconstruction algorithms for electrical capacitance tomography based on ROF model using new numerical techniques

Jiaoxuan Chen^{1,2}, Maomao Zhang¹, Yinyan Liu^{1,2}, Jiaoliao Chen³
and Yi Li^{1,4}

¹ Graduate School at Shenzhen, Tsinghua University, Shenzhen 518055, People's Republic of China

² Department of Automation, Tsinghua University, Beijing 100084, People's Republic of China

³ Key Laboratory of E&M, Ministry of Education and Zhejiang Province, Zhejiang University of Technology, Hangzhou 310014, People's Republic of China

E-mail: liyi@sz.tsinghua.edu.cn

Received 25 August 2016, revised 22 November 2016

Accepted for publication 7 December 2016

Published 2 February 2017



Abstract

Electrical capacitance tomography (ECT) is a promising technique applied in many fields. However, the solutions for ECT are not unique and highly sensitive to the measurement noise. To remain a good shape of reconstructed object and endure a noisy data, a Rudin–Osher–Fatemi (ROF) model with total variation regularization is applied to image reconstruction in ECT. Two numerical methods, which are simplified augmented Lagrangian (SAL) and accelerated alternating direction method of multipliers (AADMM), are innovatively introduced to try to solve the above mentioned problems in ECT. The effect of the parameters and the number of iterations for different algorithms, and the noise level in capacitance data are discussed. Both simulation and experimental tests were carried out to validate the feasibility of the proposed algorithms, compared to the Landweber iteration (LI) algorithm. The results show that the SAL and AADMM algorithms can handle a high level of noise and the AADMM algorithm outperforms other algorithms in identifying the object from its background.

Keywords: electrical capacitance tomography, total variation, Rudin–Osher–Fatemi model

(Some figures may appear in colour only in the online journal)

1. Introduction

Visualisation techniques, such as electrical resistance tomography (ERT), electrical capacitance tomography (ECT) and x-ray imaging, are widely applied in the petroleum, chemical and power industries. These techniques are usually used to determine phase distributions in a vessel or pipe. Compared with other tomographic techniques [1–3], ECT is a non-radioactive and non-invasive method with the advantages of low cost and high process speed. ECT can reconstruct the permittivity distributions by calculating the measured capacitances between each pair of electrodes on the periphery of the

sensing region. The quality of ECT images is mainly affected by the reconstruction algorithms. Therefore, the reconstruction algorithms play a significant role in ECT.

In past decades, many algorithms have been developed to solve ECT inverse problem, including linear back projection (LBP) [4], the Landweber iteration (LI) [5], Tikhonov regularization [6], the conjugate gradient (CG) method [7], the simultaneous iterative reconstruction technique (SIRT) [8], support vector machine (SVM) [9], the neural network algorithm [10] and so on. These algorithms are selected for specific applications in terms of a trade-off between image quality and reconstruction time. However, ECT is a soft-field technique with the non-linear relationship between the permittivity distribution and capacitance measurements. It's difficult for ECT to

⁴ Author to whom any correspondence should be addressed.

exhibit the complicated scenarios: especially a sharp transition in permittivity distribution. Moreover, image reconstruction in ECT is ill-conditioned, i.e. its result is sensitive to the measurement noise and errors.

The Rudin–Osher–Fatemi (ROF) [11] model, which is based on total variation (TV) regularization, has been proven to be extremely effective for noisy data in image processing [12–14]. Since TV regularization can allow for sharp changes in permittivity between phases, this model is used to preserve image edges and features in image restoration. Thus, some researchers have applied the ROF model to image reconstruction in ECT: Soleimani and Lionheart [15] explored a regularized Gauss–Newton scheme and found that the TV regularization could improve the separation between phases of different permittivities; Chandrasekera *et al* [16] presented an algorithm applying iterative soft thresholding (IST) to penalize the TV, which was validated using simulated data with a Gaussian noise added; Wang *et al* [17] proposed a Split–Bregman iteration (SBI) approach to solve the ECT imaging, which is of high speed and small memory footprint [12]. ECT imaging is an ill-posed problem due to the limited number of measurements, therefore applying the ROF model is still a challenge in ECT. Thus, new numerical techniques are required to be introduced for ECT by using the ROF model.

With developments in ‘compressed sensing’ [18–20], efforts have been devoted to obtain fast numerical solutions of the ROF model including the dual method [21, 22], augmented Lagrangian (AL) method [23] and accelerated alternating direction method of multipliers (AADMM) [24]. In this paper, two image reconstruction algorithms for ECT based on ROF model are proposed using the simplified augmented Lagrangian (SAL) and AADMM. Furthermore, the focus of this paper is to explore some new algorithms combined with ROF model for ECT inverse problem. The SAL and AADMM algorithms are designed as a one-step and iterative algorithm respectively in terms of the requirements in the actual case. For instance, if the computational complexity is not considered, the SAL algorithm as a one-step algorithm can be used for on-line image reconstruction because of its simplicity. Since it is almost impossible to find an accurate solution by any one-step algorithm, the AADMM algorithm can be used to obtain an accurate solution in ECT iteratively.

This paper is organized as follows: in section 2, a brief discussion of image reconstruction in ECT from the perspective of optimization and two reconstruction algorithms for ECT are proposed, inspired by the work in [20, 23, 24]; results and discussion of both simulation and experimental data are provided in sections 3 and 4 to validate the feasibility of the proposed algorithms, and section 5 concludes the paper.

2. Principle of algorithms

2.1. The regularization

In ECT, the relationship between the capacitance and permittivity distributions can be expressed as [4, 25, 26, 27],

$$\lambda = Sg \quad (1)$$

where λ is a normalized capacitance, S is a normalized matrix known as the sensitivity map, and g is the normalized permittivity.

As is well known, ECT is a soft-field problem which makes the reconstructed image smooth. Therefore, L_1 regularization methods can be exploited to reduce the smoothing effect and obtain sharper images than L_2 regularization methods. Consequently, equation (1) can be posed as an optimization problem by using L_1 regularization.

$$\min_g \frac{\mu}{2} \|Sg - \lambda\|_2^2 + \|\nabla g\|_1 \quad (2)$$

where the first term is the fidelity term with parameter μ , the second term is a TV term that includes anisotropic total variation (ATV) term $\|\nabla g\|_1 = |G_x g| + |G_y g|$ and isotropic total variation (ITV) term $\|\nabla g\|_1 = (|G_x g|^2 + |G_y g|^2)^{1/2}$. G_x and G_y are auxiliary variables which are used to calculate the horizontal and vertical gradients for g respectively. The mathematical expression for G_x and G_y can be found in the appendix [23].

2.2. SAL algorithm

AL method for ROF model is with many advantages, such as penalty method. It also has been successfully applied to nonlinear PDEs [23]. The SAL is a one-step algorithm by simplifying the AL method. The equation (2) can be initially transformed to a constrained optimization problem as follows

$$\begin{cases} \min_{g, q} \frac{\mu}{2} \|Sg - \lambda\|_V^2 + \|q\|_{1W} \\ s.t. \quad q = \nabla g \end{cases} \quad (3)$$

where $\|\cdot\|_V$ is Euclidean norm of the Euclidean space (see appendix), $\|\cdot\|_{1W}$ is 1-norm of the W space (see appendix). $q, \nabla g \in W$, are both $n \times 2$ matrices (suppose the ECT image $f(x, y)$ is an $N \times N$ matrix, where $n = N \times N$) and $\nabla g = [G_x g, G_y g]$. From equation (3), the AL function can be derived out below.

$$\begin{aligned} \text{Lar}(g, q, L) = & \frac{\mu}{2} \|Sg - \lambda\|_V^2 + \|q\|_{1W} + (L, q - \nabla g)_W \\ & + \frac{r}{2} \|q - \nabla g\|_W^2 \end{aligned} \quad (4)$$

where $(\cdot, \cdot)_W$ is inner product of the W space (see appendix), $\|\cdot\|_W$ is Euclidean norm of the W space (see appendix), L is Lagrangian multiplier, $L \in W$, is an $n \times 2$ matrix, r is a positive constant. More proof details can be found in the previous research [23]. Notice that equation (4) can be separated to the following two sub-problems, for a given q ,

$$\min_{g \in V} \frac{\mu}{2} \|Sg - \lambda\|_V^2 - (L^k, \nabla g)_W + \frac{r}{2} \|q - \nabla g\|_W^2 \quad (5)$$

and for a given g ,

$$\min_{q \in W} \|q\|_{1W} + (L^k, q)_W + \frac{r}{2} \|q - \nabla g\|_W^2 \quad (6)$$

Sub-problem (5) can be efficiently solved using Fourier transforms [13]. Defining $\mathcal{F}(\cdot)$ and $\mathcal{F}^{-1}(\cdot)$ as the Fourier transform and inverse Fourier transform respectively, the solution of g can be written as follows

$$g = \mathcal{F}^{-1} \left(\frac{\mu \mathcal{F}(S^T) \mathcal{F}(\lambda) - \mathcal{F}(G_x) \mathcal{F}(L^1)^k + r q^1 - \mathcal{F}(G_y) \mathcal{F}(L^2)^k + r q^2}{\mu \mathcal{F}(S^T) \mathcal{F}(S) - r \mathcal{F}(\Delta)} \right) \quad (7)$$

where $L = (L^1, L^2)$, $q = (q^1, q^2)$, S^T is transposed matrix of S . Δ is the Laplacian matrix, which is denoted as follows

$$\Delta = G_x^T G_x + G_y^T G_y \quad (8)$$

Note that the solution g of equation (7) is a complex number. Also, the real part of it is much larger than its imaginary part. Thus, the real part of it is chosen to represent the permittivity. Regarding the equation (6), the closed form [13] is:

$$q_{i,j} = \begin{cases} \left(1 - \frac{1}{r|h_{i,j}|}\right) h_{i,j}, & |h_{i,j}| > \frac{1}{r} \\ 0, & |h_{i,j}| \leq \frac{1}{r} \end{cases} \quad (9)$$

where $1 \leq i \leq n$, $1 \leq j \leq 2$, and h is denoted as below.

$$h = \nabla g - \frac{L^k}{r} \quad (10)$$

Finally Lagrangian multiplier L is updated by:

$$L^{k+1} = L^k + r(q^k - \nabla g^k) \quad (11)$$

In fact, the AL method can be simplified by setting the variables L and q to zeroes. Therefore, the equation (7) can be simplified as below.

$$g = \mathcal{F}^{-1} \left(\frac{\mu \mathcal{F}(S^T) \mathcal{F}(\lambda)}{\mu \mathcal{F}(S^T) \mathcal{F}(S) - r \mathcal{F}(\Delta)} \right) \quad (12)$$

Through this method, which is called the SAL algorithm, the permittivity g is calculated easily from equation (12). The main computational time in SAL algorithm involves four FFT and one inverse FFT. The SAL algorithm is shown in algorithm 1 explicitly.

Algorithm 1. SAL

1. Input: sensitivity matrix S , capacitance measurements λ , μ , r ;
 2. Obtain g by solving equation (12);
 3. Output: real part of g .
-

2.3. AADMM algorithm

The basic idea of AADMM is to transform a constrained optimization problem to a series of unconstrained problems. Moreover, the AADMM algorithm is simply alternating direction method of multipliers (ADMM) with a predictor-corrector-type acceleration step. In the ECT imaging, the acceleration used in AADMM is of the form first presented in [16]. As a matter of fact, the AADMM algorithm is close to the SAL algorithm when the parameters used in the two algorithms are selected properly [23, 24].

For equation (1), a common optimized formulation using AADMM solves the following

$$\begin{cases} \min_{g,p} \frac{\mu}{2} \|Sg - \lambda\|_V^2 + \|p\|_W + \frac{\varepsilon}{2} \|p\|_W^2 \\ \text{s.t. } p = \nabla g \end{cases} \quad (13)$$

where the third term in the first row is an L_2 regularization term with a smoothing parameter ε .

By decomposing the equation (13), the L_1 and L_2 components are split into two sub-problems using the generalized ADMM method. To find the optimal number of g , the following sub-problem must be solved firstly

$$g^k = \arg \min_g \left(\frac{\mu}{2} \|Sg - \lambda\|_V^2 + (d^k, -\nabla g)_W + \frac{\tau}{2} \|s^k - \nabla g\|_W^2 \right) \quad (14)$$

where d and s are auxiliary variables, τ is a positive constant. The right side of equation (14) is obviously a quadratic programming problem and it's easy to gain the optimal value:

$$(\tau \Delta + \mu S^T S) g^{k+1} = \mu S^T \lambda + \nabla \cdot (d^k + \tau s^k) \quad (15)$$

where $\nabla \cdot$ is a divergence operator.

Note that equation (15) [24] is a typical linear problem. Since the CG method is computed rapidly when applied to large-size problems, this method is utilized to require g^k [17].

The another sub-problem is expressed as,

$$p^k = \arg \min_p \left(\|p\|_W + \frac{\varepsilon}{2} \|p\|_W^2 + (d^k, p)_W + \frac{\tau}{2} \|p - \nabla g^k\|_W^2 \right) \quad (16)$$

It's available to take the advantage of a generalized shrinkage formula to deal with equation (16) [24] for p^k .

$$p^k = \text{shrink} \left(\frac{\tau}{\tau + \varepsilon} (\nabla g^k + \tau d^k), \frac{1}{\tau + \varepsilon} \right) \quad (17)$$

where the i th element of the shrinkage formula can be denoted as,

$$\text{shrink}(z, v)_i = \frac{z_i}{|z_i|} \max\{|z_i| - v, 0\} \quad (18)$$

The AADMM algorithm is summarized in algorithm 2. Moreover, the acceleration step [24] in the AADMM algorithm is introduced explicitly in algorithm 2.

Algorithm 2. AADMM

1. Input: sensitivity matrix S , capacitance measurements λ , μ , ε , τ ;
 2. Initialize: $p^{-1} = s^0 \in W$, $c^{-1} = d^0 \in W$ and $g \in V$ with zeros, $\alpha^1 = 1$;
 3. While $\|g^k - g^{k-1}\|_2 < \text{tol}$
 - (1) Obtain g^k by solving equation (15) using the CG method;
 - (2) Obtain p^k by solving generalized shrinkage formula in equation (17);
 - (3) $c^k = d^k + \tau(p^k - \nabla g^k)$;
 - (4) $\alpha^{k+1} = \frac{1 + \sqrt{1 + 4(\alpha^k)^2}}{2}$;
 - (5) $s^{k+1} = p^k + \frac{\alpha^k - 1}{\alpha^{k+1}}(p^k - p^{k-1})$;
 - (6) $d^{k+1} = c^k + \frac{\alpha^k - 1}{\alpha^{k+1}}(c^k - c^{k-1})$;
 - end
 4. Output: permittivity g .
-

3. Simulation results

In this section, the simulations are carried out to evaluate the performance of the proposed SAL and AADMM algorithms.

3.1. Modelling

The ECT simulation model is shown in figure 1. The inner and external radius of this eight-electrode sensor is 35 mm and 40 mm respectively. The commercial software (COMSOL Multiphysics) is used to generate the mathematical grids (64×64) of a 2D model (see figure 1) and solve the discrete electrical field using finite element method (FEM). Three distributions are chosen for the simulation: cross-shaped, 'V'-shaped and two rectangular-shaped, as shown in figure 2. The three objects are constructed in an air (relative permittivity 1) background with oil (relative permittivity 2.3) as a high permittivity material. The reconstruction is completed using MATLAB R2015b on a PC with an Intel Core i5-6400 2.7 GHz CPU and 4 GB of RAM.

3.2. Reconstruction

3.2.1. Parameter settings. The relaxation factor and the number of iteration for LI are chosen to be 0.004 and 5000 respectively in all our tests. The parameters used in the SAL and AADMM algorithms varies for the different distributions. In the SAL algorithm, the parameter μ is set as 1 while the parameter $r \in [1, 100]$. In the AADMM algorithm, the parameter ε is chosen to be 0.01 while the parameters μ and τ are

set as $\begin{cases} \mu = 500 \\ \tau = 1 \end{cases}$ or $\begin{cases} \mu = 0.5 \\ \tau \in [1, 10] \end{cases}$. Moreover, if μ is far greater

than τ (e.g. $\mu = 500$ and $\tau = 1$), the results of the AADMM

algorithm in the first iteration are very close to those of the SAL algorithm ($r = 1$).

3.2.2. Results. For cross-shaped distribution, the figure 3(b) presents that the central area of image reconstructed by LI is apparently distorted and the boundary of it is rough. While in figures 3(c) and (d), the SAL and AADMM algorithms benefit from the introduction of TV penalization and can both preserve more edge characteristics of the object, e.g. a specific and smooth boundary of the object.

For 'V'-shaped distribution, figures 3(f) and (h) show that the LI algorithm tends to smooth out the boundary between the object and its background while the AADMM algorithm has a sharper transition in permittivity. It is worth noting that the AADMM reconstruction makes demarcation of the object from background clear and shows a good quantification of permittivity values. Figures 3(f) and (g) illustrate that the TV term in equation (2) has a little effect on the result of the SAL algorithm. After all, the SAL is a one-step algorithm.

For two rectangular-shaped distribution, figures 3(j), (k) and (l) illustrate that the SAL and AADMM algorithms both can remain good shape of the object. In addition, the

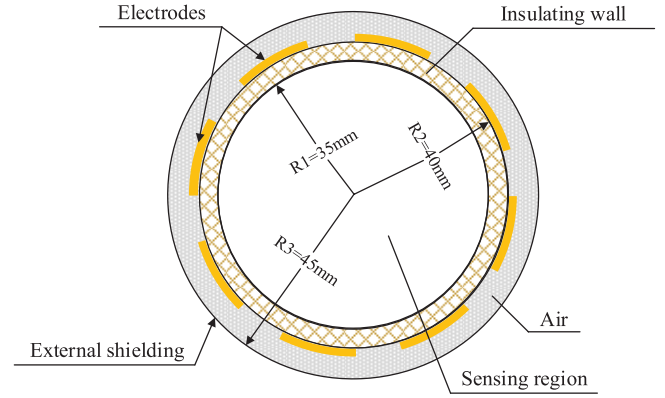


Figure 1. Structure diagram of 2D ECT model.

figure 3(j) provides that the two rectangles trend to be connected together. It can be found that the three images all possess a distortion at different level. However, the AADMM algorithm outperforms the best with a better image contrast.

Figure 4 shows the results of the SAL and AADMM algorithms using corresponding parameters. It is observed that the difference between the SAL and AADMM is negligible. Compared with the LI algorithm in figure 3, it can be found that the TV regularization is with a slight effect on the SAL and AADMM algorithms, particularly for the 'V'-shaped and two rectangular-shaped distributions.

The relative mean error and standard deviation, which are shown in equations (19) and (20) respectively, are used to evaluate the performance of each iteration of the AADMM algorithm. In order to focus on the region of objects, the reconstructed permittivity values beyond the interesting sensing area are configured as zero artificially.

$$\sigma = \sqrt{\frac{1}{M} \sum_{i=1}^M (g_i - g_0)^2}$$

$$g_0 = \frac{1}{M} \sum_{i=1}^M g_i \quad (19)$$

$$\theta = \frac{g_0 - g_t}{g_t} \times 100\% \quad (20)$$

where σ is the standard deviation, M is the total number of pixels in the area which close to the objects, g_i is the reconstructed permittivity value, g_0 is the mean value of reconstructed image and g_t is the mean value of true image. θ is the relative mean error.

Figure 5(a) illuminates that the AADMM algorithm can extract demarcation of the object from background effectively. In addition, figure 5(b) illustrates that the AADMM algorithm can successfully distinguish the two rectangles from each other. Figure 6 shows the relative mean error and standard deviation of the results corresponding to the figure 5. As shown in figure 6, the relative mean error tends to be increased with the increases of the number of iterations. Meanwhile, the standard deviation has a tendency to decline.

Generally, the standard deviation plays a more important role in determining the number of the AADMM algorithm. From the figures 5 and 6, it can be found that the AADMM

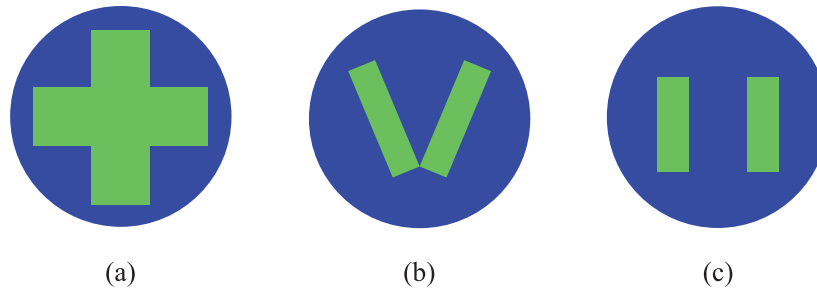


Figure 2. Simulated inclusions: (a) cross-shaped, (b) 'V'-shaped and (c) two rectangular-shaped.

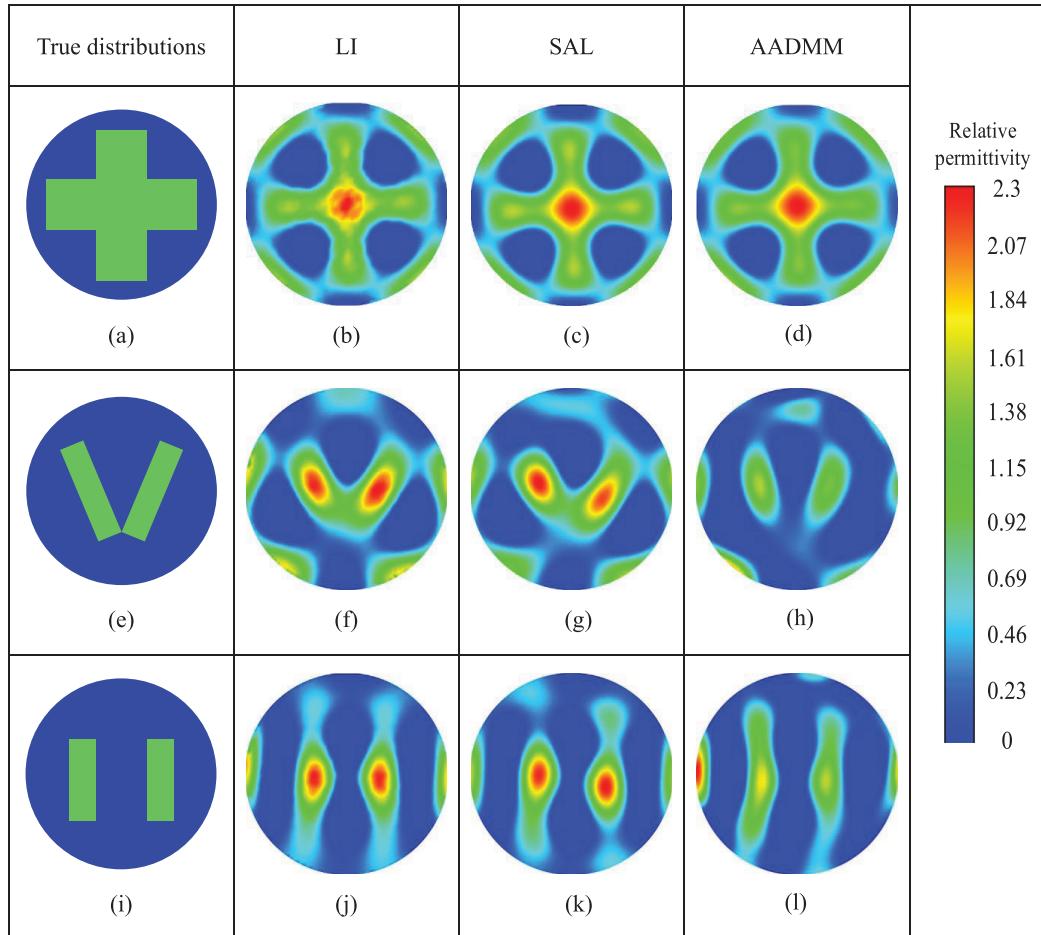


Figure 3. Images reconstructed from the simulated data. (a) cross-shaped, (b) $r = 1$, (c) $\mu = 0.5$, $\tau = 2$, (d) 'V'-shaped, (e) $r = 40$, (f) $\mu = 0.5$, $\tau = 5$, (g) two rectangular-shaped, (h) $r = 40$, (i) $\mu = 0.5$, $\tau = 5$. The relaxation factor used in the LI is 0.004 for all three distributions.

can identify the object from its background better with the standard deviation decreasing. That is to say, a smaller standard deviation implies a more uniform distribution image. Furthermore, a smaller relative mean error indicates that the permittivity distribution is closer to the actual case.

3.3. Imaging time and effect of noise level

As shown in table 1, although the number of iteration for the LI algorithm is much larger than that for the other algorithms, it takes the shortest time among the three algorithms. The elapsed time of the SAL algorithm is independent of the permittivity distributions. Once the sensor is determined, the

sensitivity map S is constant. Thus except for capacitance λ , all quantities are constant in equation (12). The computation time in the SAL algorithm is mainly consumed by one FFT and one inverse FFT, once the constant quantities are computed in advance. Normally, it can save the running time of the SAL algorithm more than 28.14% in the tests.

To examine the ability of proposed algorithms for better corner detection at different noise level, a Gaussian noise is added to the normalized capacitance measurements and the suitable signal-to-noise ratio (SNR) is chosen with respect to different inclusions. The SNR for the cross-shaped, 'V'-shaped and two rectangular-shaped is 30 dB, 25 dB and 17 dB respectively.

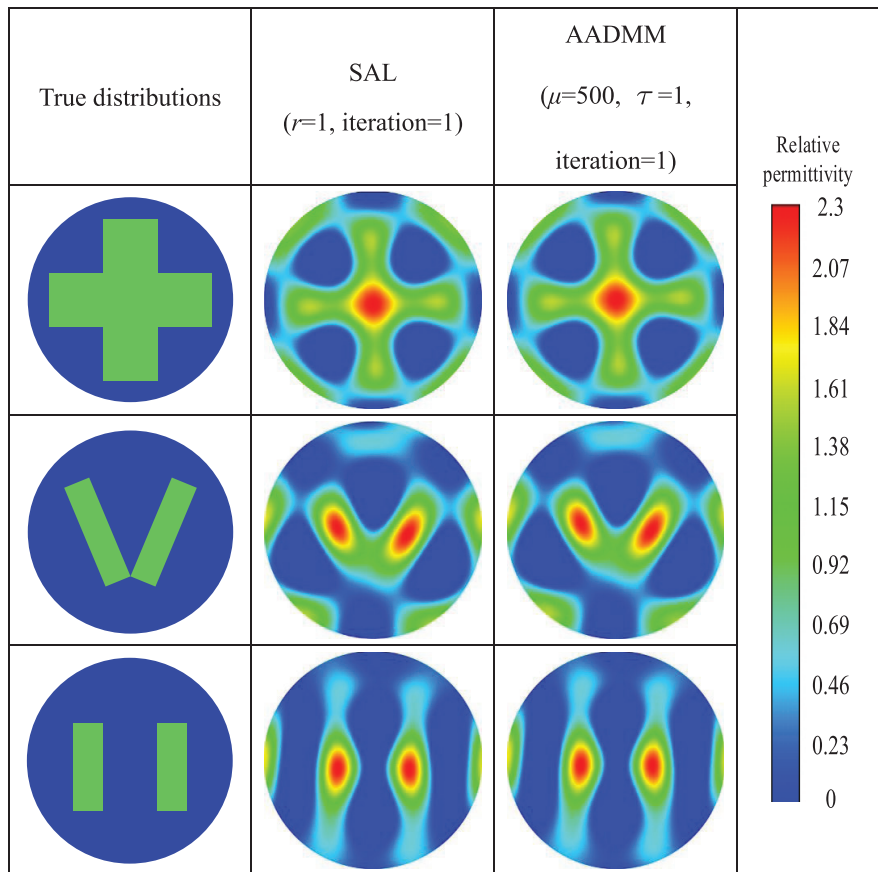


Figure 4. Images reconstructed by the SAL and AADMM algorithms with corresponding parameters.

Figure 7 shows all images possess a kind of distortion at different level compared with the corresponding images in figure 3. Obviously, the AADMM algorithm outperforms better than the rest of algorithms. More specifically, figure 7(d) provides that the AADMM algorithm can remain the shape of permittivity distribution. Figures 7(h) and (l) show that the AADMM algorithm is capable of identifying the objects from background efficiently. Similar to the figures 3(b), (c) and (f), (g), figures 7(b), (c) and (f), (g) show the SAL algorithm has a slight effect on the images except for the figure 7(c). From figures 7(j), (k) and (l), it can be found that the SAL and AADMM algorithms can endure a relatively high level of noise and improve the quality of images. Naturally, the noise tend to weaken the ability of the SAL and AADMM algorithms for better corner detection.

4. Experimental results

Static experiments were carried out to validate the performance of proposed algorithms using an ECT system with an eight-electrode sensor. The data acquisition speed of the data acquisition system is about 350 Hz, i.e. the data acquisition system can obtain about 350 sets of capacitance data of

28 electrodes pairs per second. The SNRs of capacitance data for each of 28 electrodes pairs ranged from 30 dB to 40 dB. In order to avoid the system errors and noises, the average of thousands of frames is used as the capacitance data.

As shown in figure 8, the diameter of the ECT sensor was 76 mm and the angular span of each electrode was 30°. The samples of the same shape used in the simulation were utilized for the experimental test (see figure 9). Air and dry sand were used as the low and high permittivity materials (relative permittivity 1 and 4 respectively) to calibrate the system. Paper-made containers in different shapes are filled with dry sand, which represent for each tested distribution.

Figure 10 shows the experimental results perform similarly to the simulation test, and the AADMM algorithm provides better image quality in terms of the image contrast and the shape of the object:

- Figures 10(b)–(d) illustrate that the central area of image reconstructed by the LI algorithm is obviously distorted and the edge of the object is rough. Meanwhile the AADMM algorithm can retain the shape of the object better than the SAL algorithm.
- Figures 10(f) and (h) provide that the LI algorithm cannot distinguish the edge of the object, meanwhile the

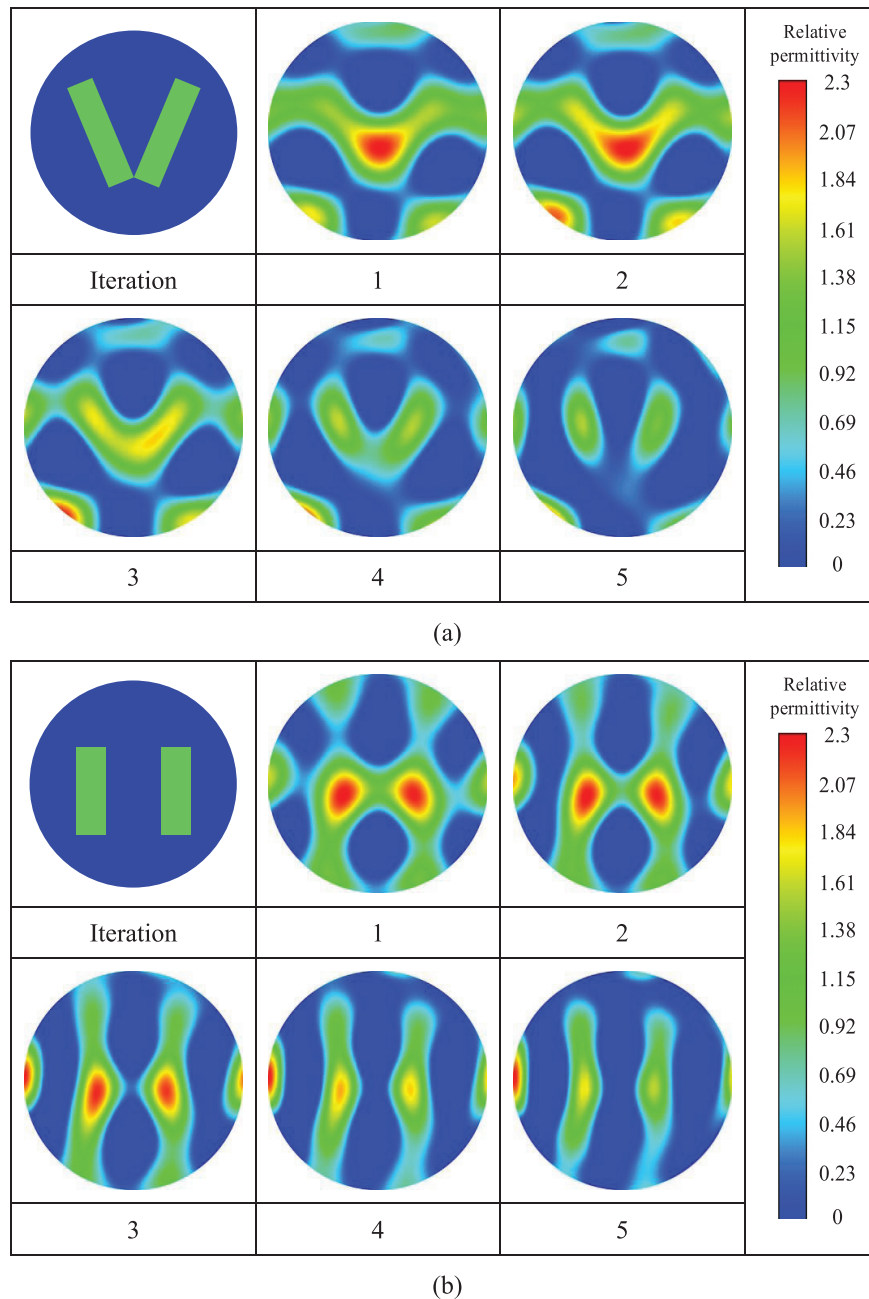


Figure 5. Intermediate results of the AADMM ($\mu = 0.5$ and $\tau = 5$) algorithm with a different number of iterations: (a) 'V'-shaped distribution; (b) two rectangular-shaped distribution.

Table 1. Elapsed time (in seconds).

Distributions	LI	SAL	AADMM
Cross-shaped	1.25	5.34	4.88
'V'-shaped	1.19	5.52	8.78
Two rectangular-shaped	1.23	5.49	8.56

AADMM algorithm can identify the object from background evidently, a low intensity 'bridge' is formed inside the object though.

- Figure 10(j) indicates that the two rectangles have a tendency to be connected together, which is similar to the case in figure 3. Figure 10(l) demonstrates that the image reconstructed by the AADMM algorithm has a good image contrast.

5. Summary

In this paper, two image reconstruction algorithms for ECT based on ROF model are introduced preliminarily. The two

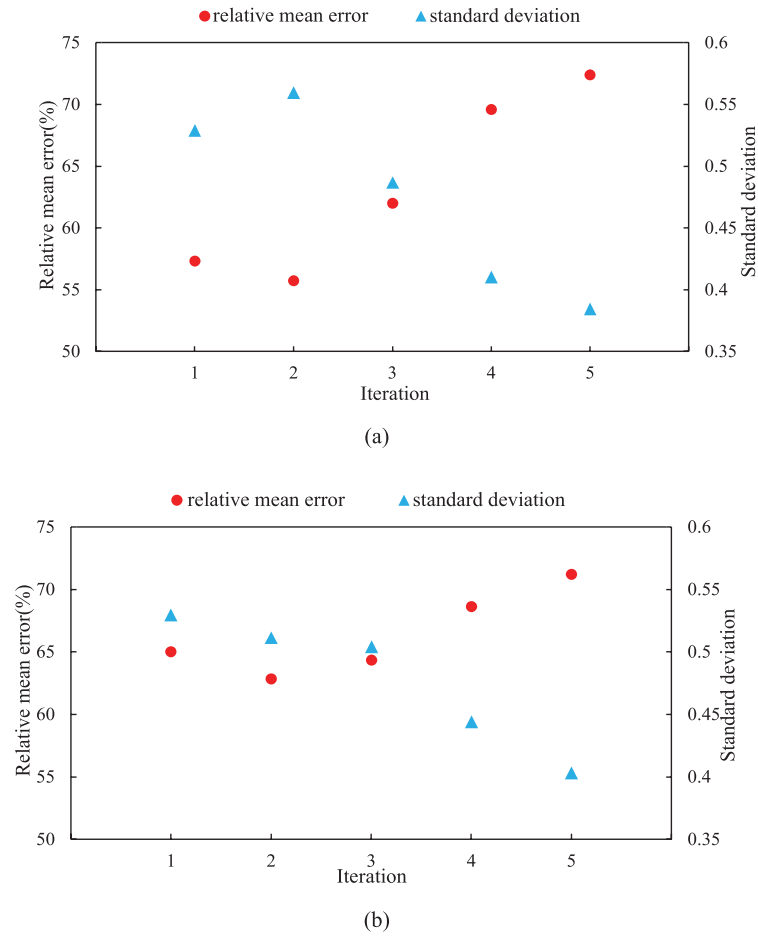


Figure 6. The relative mean error and standard deviation of the results reconstructed by the AADMM ($\mu = 0.5$ and $\tau = 5$) algorithm with a different number of iterations: (a) 'V'-shaped distribution; (b) two rectangular-shaped distribution.

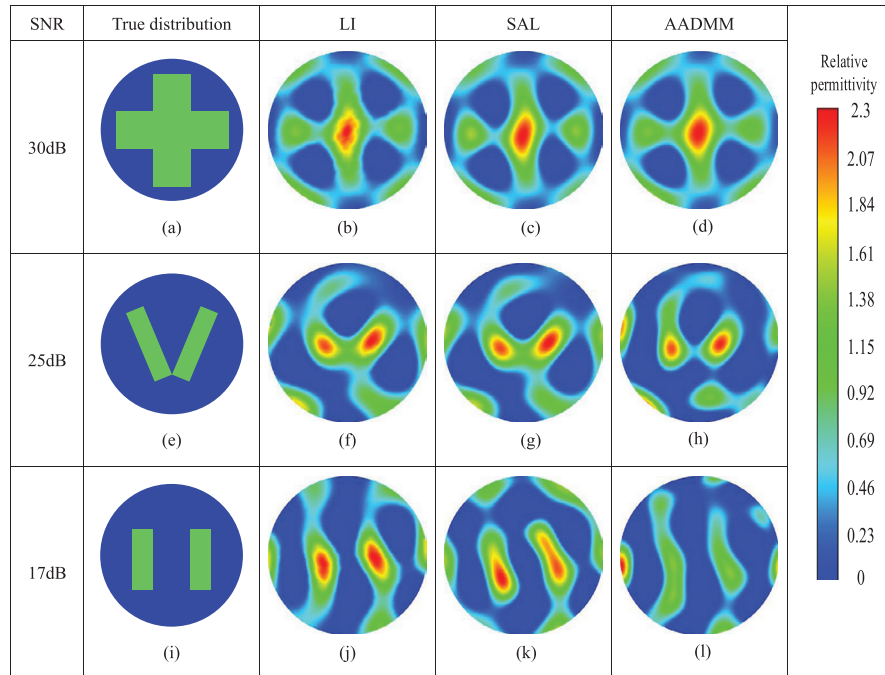


Figure 7. Images reconstructed from the noisy data. The normalized capacitance are added with Gaussian noise such that the signal-to-noise ratio (SNR) for the cross-shaped, 'V'-shaped and two rectangular-shaped distributions are 30 dB, 25 dB and 17 dB respectively. (a) cross-shaped, (b) $r = 1$, (c) $\mu = 0.5, \tau = 2$, (d) 'V'-shaped, (e) $r = 1$, (f) $\mu = 0.5, \tau = 0.5$, (g) two rectangular-shaped, (h) $r = 80$, (i) $\mu = 0.5, \tau = 5$. The relaxation factor used in the LI is 0.004 for all three distributions.

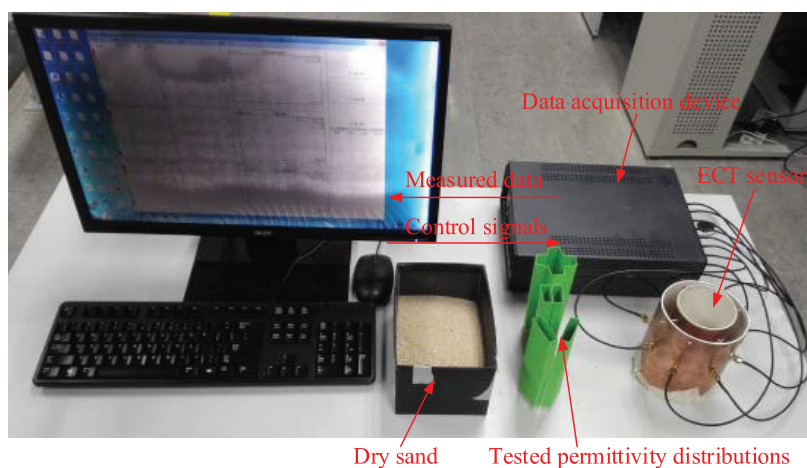


Figure 8. ECT system and materials used in the experimental study.

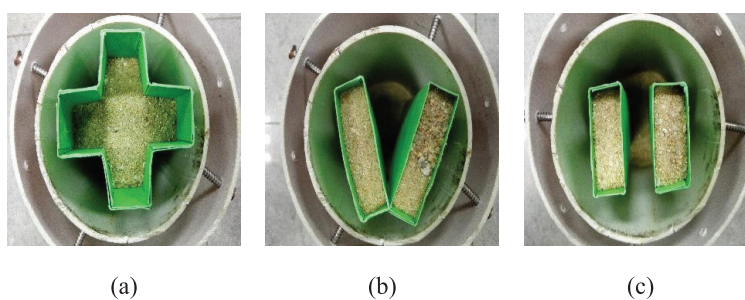


Figure 9. Real permittivity distributions used in the experimental study : (a) cross-shaped, (b) 'V'-shaped and (c) two rectangular-shaped.

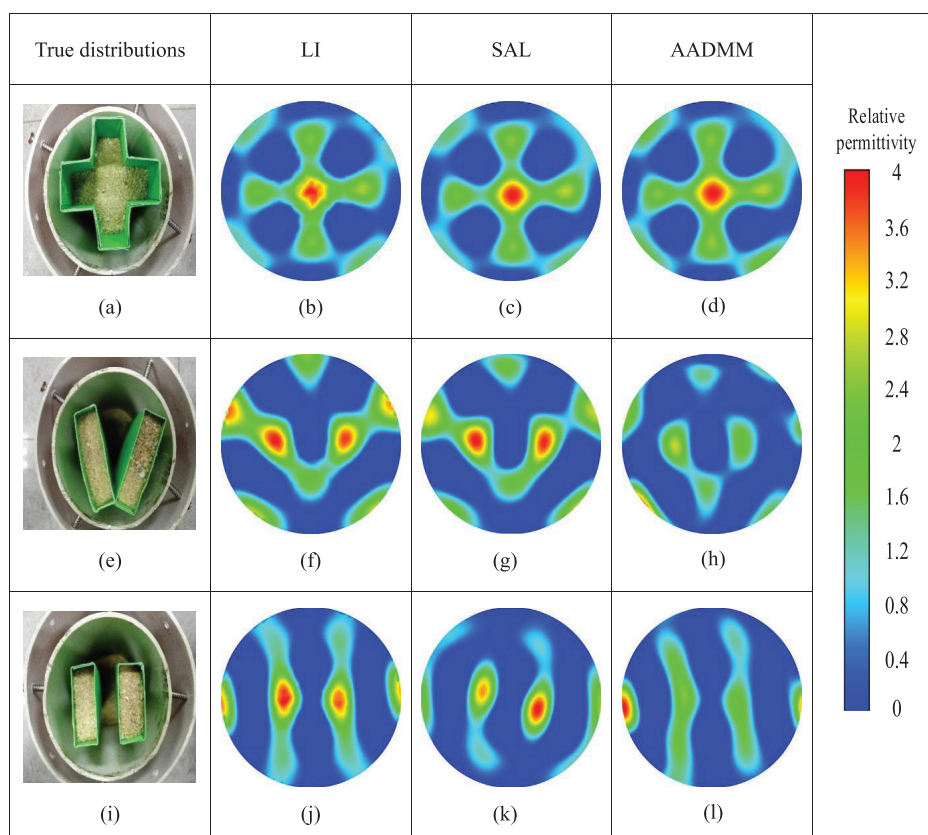


Figure 10. Images reconstructed from the experimental data. (a) cross-shaped, (b) $r = 1$, (c) $\mu = 0.5$, $\tau = 1$, (d) 'V'-shaped, (e) $r = 40$, (f) $\mu = 0.5$, $\tau = 2$, (g) two rectangular-shaped, (h) $r = 70$, (i) $\mu = 0.5$, $\tau = 5$. The relaxation factor used in the LI is 0.004 for all three distributions.

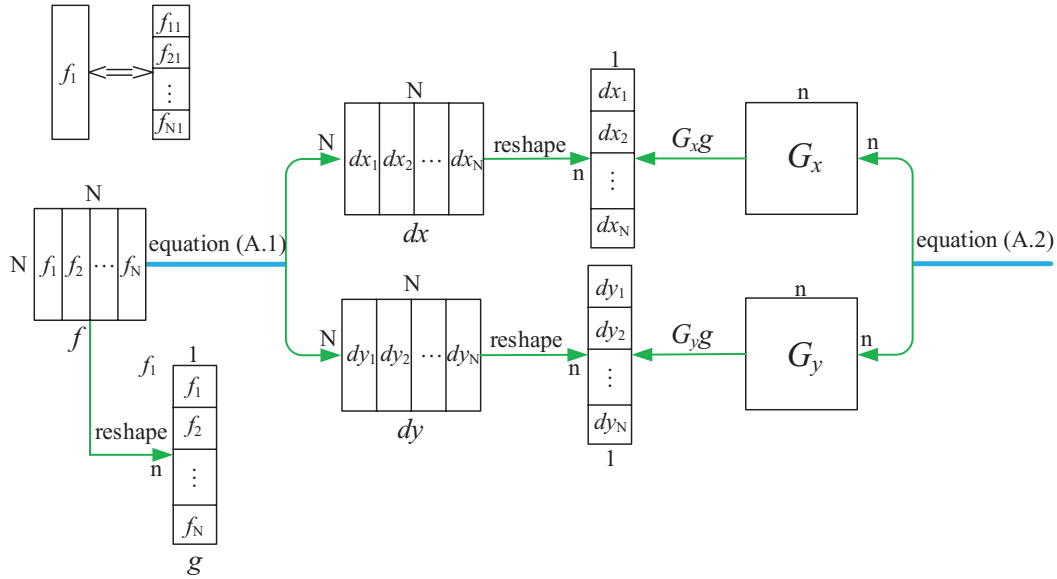


Figure A1. Relationships among the variables.

algorithms are designed as a one-step and iterative algorithms, i.e. the SAL for one-step and the AADMM for iterative algorithms. Both simulation and experimental tests were carried out to validate the feasibility of the proposed algorithms. The results show that the SAL and AADMM algorithms can make the boundary of the object clear in several cases. Moreover, the AADMM algorithm is good at distinguishing objects from the background, such as two rectangular-shaped and 'V'-shaped. Furthermore, the two algorithms can endure a relatively high level of noise and improve the quality of images, particularly the AADMM algorithm. Naturally, the noise tend to weaken the ability of the two algorithms for better corner detection.

The results also indicate that some images reconstructed by the SAL are similar to those of the LI. After all, the SAL is a one-step algorithm. Also, some artifacts in the images reconstructed by the AADMM cannot be removed. In future work, the results of the AADMM algorithm could be discussed and improved further with more experiment and simulation but not present in this paper.

Acknowledgments

The authors would like to thank the National Natural Science Foundation of China (No.61571252) and the internal grant of

Tsinghua University Shenzhen Graduate School (050100001) for supporting this work.

Appendix

This appendix describes how to get G_x and G_y , and gives some basic notations.

The Euclidean space $R^{N' \times N'}$ is denoted as V . Without the loss of generality, suppose the ECT image $f(x, y)$ is an $N \times N$ matrix, where $n = N \times N$. The f can be stored as an $n \times 1$ vector g in which each element corresponds to a pixel in the ECT imaging region. It makes sense to consider $g \in V$ accordingly. The dx and dy are defined as horizontal and vertical gradients for f respectively using forward difference approximation.

For $1 \leq i, j \leq N$,

$$\begin{aligned} (dx)_{i,j} &= \begin{cases} f_{i,j+1} - f_{i,j}, & 1 \leq j \leq N-1 \\ f_{i,1} - f_{i,N}, & j = N \end{cases} \\ (dy)_{i,j} &= \begin{cases} f_{i+1,j} - f_{i,j}, & 1 \leq i \leq N-1 \\ f_{1,j} - f_{N,j}, & i = N \end{cases} \end{aligned} \quad (\text{A.1})$$

$$\begin{aligned} (G_x)_{(j-1) \times N + i, J} &= \begin{cases} -1, & J = (j-1) \times N + i, & 1 \leq j \leq N \\ 1, & J = i, & j = N \\ 1, & J = j \times N + i, & 1 \leq j \leq N-1 \end{cases} \\ (G_y)_{(j-1) \times N + i, J} &= \begin{cases} -1, & J = (j-1) \times N + i, & 1 \leq i \leq N \\ 1, & J = (j-1) \times N + 1, & i = N \\ 1, & J = (j-1) \times N + i + 1, & 1 \leq i \leq N-1 \end{cases} \end{aligned} \quad (\text{A.2})$$

The remaining elements of G_x and G_y are all set to zeroes. The relationships among the variables aforementioned are shown in figure A1.

The usual inner product and Euclidean norm of space V are denoted as $(\cdot, \cdot)_V$ and $\|\cdot\|_V$ respectively. The space W is equipped with inner product $(\cdot, \cdot)_w$ and Euclidean norm $\|\cdot\|_w$,

which are determined as follows. For $T, P \in W$, are both $n \times 2$ matrices,

$$(T, P)_W = (T^1, P^1)_V + (T^2, P^2)_V \quad (\text{A.3})$$

where T^1 and T^2 and P^1 and P^2 are the first and second column of T and P respectively, and

$$\|T\|_W = \sqrt{(T, T)_W} \quad (\text{A.4})$$

References

- [1] Wang M, Ramskill N P, Barns S, Raynel G, Qiu C H and Rayner C M 2013 A feasible process tomography and spectroscopy measurement system to determine carbon dioxide absorption *Flow Meas. Instrum.* **31** 77–85
- [2] Schleicher E, Silva M J D, Thiele S, Li A, Wollrab E and Hampel U 2008 Design of an optical tomograph for the investigation of single- and two-phase pipe flows *Meas. Sci. Technol.* **19** 094006
- [3] Sun J T and Yang W Q 2013 Fringe effect of electrical capacitance and resistance tomography sensors *Meas. Sci. Technol.* **24** 074002
- [4] Yang W Q and Peng L H 2003 Image reconstruction algorithms for electrical capacitance tomography *Meas. Sci. Technol.* **14** R1–13
- [5] Li Y and Yang W Q 2008 Image reconstruction by nonlinear Landweber iteration for complicated distributions *Meas. Sci. Technol.* **19** 094014
- [6] Peng L H, Merkus H and Scarlett B 2000 Using regularization methods for image reconstruction of electrical capacitance tomography *Part. Part. Syst. Charact.* **17** 96–104
- [7] Wang Q, Yang C Y, Wang H X, Cui Z Q and Gao Z T 2013 Online monitoring of gas–solid two-phase flow using projected CG method in ECT image reconstruction *Particuology* **11** 204–15
- [8] Su B L, Zhang Y H, Peng L H, Yao D Y and Zhang B F 2000 Simultaneous iterative reconstruction technique for electrical capacitance tomography *Chem. Eng. J.* **77** 37–41
- [9] Chen X, Hu H L, Liu F and Gao X X 2011 Image reconstruction for an electrical capacitance tomography system based on a least-squares support vector machine and a self-adaptive particle swarm optimization algorithm *Meas. Sci. Technol.* **22** 104008
- [10] Warsito W and Fan L S 2001 Neural network based multi-criterion optimization image reconstruction technique for imaging two- and three-phase flow systems using electrical capacitance tomography *Meas. Sci. Technol.* **12** 323
- [11] Rudin L I, Osher S and Fatemi E 1992 Nonlinear total variation based noise removal algorithms *Physica D* **60** 259–68
- [12] Goldstein T and Osher S 2009 The Split Bregman method for L_1 -regularized problems *SIAM J. Imaging Sci.* **2** 323–43
- [13] Wang Y L, Yang J F, Yin W T and Zhang Y 2008 A new alternating minimization algorithm for total variation image reconstruction *SIAM J. Imaging Sci.* **1** 248–72
- [14] Zulfiquar M, Bhotto A, Ahmad M O and Swamy M N S 2015 An improved fast iterative shrinkage thresholding algorithm for image deblurring *SIAM J. Imaging Sci.* **8** 1640–57
- [15] Soleimani M and Lionheart W R B 2005 Nonlinear image reconstruction for electrical capacitance tomography using experimental data *Meas. Sci. Technol.* **16** 014
- [16] Chandrasekera T C, Li Y, Dennis J S and Holland D J 2012 Total variation image reconstruction for electrical capacitance tomography *Proc. IEEE Int. Workshop on Imaging Systems and Techniques* pp 584–9
- [17] Wang H C, Fedchenia I, Shishkin S L, Finn A, Smith L L and Colket M 2015 Sparsity-inspired image reconstruction for electrical capacitance tomography *Flow Meas. Instrum.* **43** 59–71
- [18] Yin W T, Osher S, Goldfarb D and Darbon J 2008 Bregman Iterative algorithms for L_1 -minimization with applications to compressed sensing *SIAM J. Imaging Sci.* **1** 143–68
- [19] Becker S, Bobin J and Candès E J 2011 NESTA: a fast and accurate first-order method for sparse recovery *SIAM J. Imaging Sci.* **4** 1–39
- [20] Donoho D L 2006 Compressed sensing *IEEE Trans. Inf. Theory* **52** 1289–306
- [21] Chan T F, Golub G H and Mulet P 1999 A nonlinear primal-dual method for total variation-based image restoration *SIAM J. Sci. Comput.* **20** 1964–77
- [22] Chambolle A 2009 An algorithm for total variation minimization and applications *J. Math. Imaging Vis.* **20** 89–97
- [23] Wu C and Tai X C 2010 Augmented Lagrangian method, dual methods, and Split Bregman iteration for ROF, vectorial TV, and high order models *SIAM J. Imaging Sci.* **3** 300–39
- [24] Goldstein T, O'Donoghue B, Setzer S and Baraniuk R 2014 Fast alternating direction optimization methods *SIAM J. Imaging Sci.* **7** 1588–623
- [25] Li Y, Yang W Q, Xie C G, Huang S M, Wu Z P, Tsamakis D and Lenn C 2013 Gas/oil/water flow measurement by electrical capacitance tomography *Meas. Sci. Technol.* **24** 074001
- [26] Li Y and Holland D J 2013 Fast and robust 3D electrical capacitance tomography *Meas. Sci. Technol.* **24** 105406
- [27] Zhang M and Soleimani M 2016 Simultaneous reconstruction of permittivity and conductivity using multi-frequency admittance measurement in electrical capacitance tomography *Meas. Sci. Technol.* **27** 025405